

Boundary Layer Ingestion Noise and Turbulence Scale Analysis at High and Low Advance Ratios

David Wisda¹, W. Nathan Alexander², and William Devenport³
Virginia Tech, Blacksburg VA 24061

Stewart A. L. Glegg⁴
Florida Atlantic University, Boca Raton FL 33431

Far field sound has been measured at several receiving angles from a rotor partially embedded in a boundary layer. The haystacking pattern, or spectral humps that appear at multiples of the blade passage frequency, was studied for a wide range of advance ratios. At high advance ratios, evidence of vortex shedding from the blade trailing edges was observed. For low advance ratios, the haystacks narrowed, became more symmetric and increased in number. A method of determining the average acoustic signature of an eddy passage through a rotor was developed from time delay aligning multiple microphone signals and eddy passages detected using a short time Fourier transform. This detection technique was expanded upon through the use of the continuous wavelet transform. It was found that the eddy passage signatures were similar to a cosine wave with a Gaussian window. It was also found that normalized timescales obtained directly from the eddy passage signatures remained constant with advance ratio. A method of determining lateral timescales from the autocorrelation function of the eddy passage signatures was also developed. It was found that normalized lateral scales also remained constant with advance ratio. For advance ratios less than 0.6, the eddy passage signatures were dominated by a tonal component.

I. Introduction

Haystacking is broadband rotor noise produced by coherent blade-to-blade turbulence interaction. This phenomenon was first observed by Sevik (1971) while studying the broadband noise produced by the ingestion of grid-generated turbulence. He measured the unsteady axial force of a 10-blade rotor and observed lumps at the blade passage frequency and its harmonics. His broadband noise prediction methods did not account for blade-to-blade coherence and therefore omitted this feature.

Since Sevik's study much work has focused on turbulence ingestion noise which includes blade-to-blade coherence. Majumdar and Peake (1998) investigate haystacking noise at static and in flight conditions from the ingestion of atmospheric turbulence. At in flight conditions, the turbulence distortion is weak and haystacking was not observed. They show that static tests often produce significant haystacking noise because of the turbulent distortion of coherent structures into long thin filaments. These filaments are cut many times and produce significant noise that is highly tonal at static conditions. Although the haystacking noise may be minimal for isotropic flows with short streamwise timescales, the same cannot be assumed for the anisotropic case with significant distortion.

Stephens and Morris (2009) performed acoustic and turbulent velocity measurements of a rotor ingesting a thin casing boundary layer. In this case, the flow was anisotropic, but was axially symmetric. The thin boundary layer covered only the outer 13% of the blade tips. They used the same rotor design as Sevik operating at advance ratios of 0.47 to 1.35. Acoustic measurements were compared to predictions which used a modeled two-point turbulence correlation function. This correlation function was based on a subset measurement of the two-point turbulence statistics of the boundary layer. Their predictions also assumed that the approach turbulence was not distorted by the rotor, but were successful in determining the haystacking peak magnitude and decay. They attribute the deficiencies in their predictions to inaccurately representing the true approach turbulence statistics with a model derived from limited measurement of the undistorted flow.

¹ Graduate Student, Department of Aerospace and Ocean Engineering, AIAA Student Member.

² Research Scientist, Department of Aerospace and Ocean Engineering, AIAA Member.

³ Professor, Department of Aerospace and Ocean Engineering, AIAA Associate Fellow.

⁴ Professor, Department of Ocean Engineering, AIAA Associate Fellow.

Alexander *et al.* (2013) present the noise produced by a 2.25 scaled version of Sevik's rotor ingesting a highly inhomogeneous, anisotropic thick planar turbulent boundary layer flow. The boundary layer in this case covered as much as 50% of the blade span. To investigate the distortion of the turbulence as it was stretched into the rotor plane, they perform a turbulent scale analysis using the measured far field noise alone. A time frequency distribution was used to calculate an integral time scale of the noise produced at the blade passage frequency (BPF). The time extent of this noise was directly related to the streamwise extent of the ingested turbulence and showed a contraction of the time scale with increased thrust. A lateral turbulence scale analysis was investigated using the mean spectral haystacking peak decay. They used a Gaussian function to simulate the acoustic response of a single blade to a turbulent eddy. The width of the Gaussian function was used to fit the spectral decay, but underpredicted the measured haystack peak magnitudes at higher harmonics. Nonetheless, this indicated a lateral scale that did not vary with thrusting condition.

This study is an expansion of the experimental work and analysis described in Alexander *et al.* (2013). Measurements were performed over a broader range of rotor operating conditions and noise spectra are presented covering a large range of advance ratios. The evolution of the character of the noise spectra from a zero-thrust case to thrusting is investigated as well as the influence of varying boundary layer thickness. As an extension of Alexander *et al.* (2013), the turbulence structure is investigated by analysis of the time frequency distribution of the noise using a much expanded set of acoustic data. The acoustic signature of ingested coherent turbulence structures is analyzed using the acoustic time series measured by individual microphones. Typical eddy signatures are deduced and used to estimate time average scales of the turbulence passing through the rotor.

II. Apparatus and Instrumentation

A. Wind Tunnel

This experiment was conducted in the Virginia Tech Stability Wind Tunnel in its hemi-anechoic configuration diagramed in Figure 1. This arrangement has been used in previous experiments (Alexander *et al.* (2013), Meyers *et al.* (2013)) in which the starboard acoustic window of the tunnel's anechoic test section is replaced with a hard wall made of six Lexan panels. These panels were adjusted to ensure zero-pressure gradient. The port wall is a tensioned Kevlar fabric which contains the flow but is acoustically transparent. This creates an acoustic window 5.14 m long and 1.83 m high behind which acoustic measurements can be performed thus eliminating any microphone self-noise. An anechoic chamber, effective down to a frequency of 180Hz, flanks the port side wall isolating the acoustic instrumentation from ambient noise in the tunnel control room. The floor and ceiling of the test section are made of Kevlar stretched over 2'x2' metal perforate panels backed by foam wedges.

Two trip configurations were used to produce boundary layers of varying thickness on the Lexan wall. To create an approximately 101 mm thick boundary layer a single 9.5 mm tall trip was placed 1.35 m upstream of the start of the test section in the contraction. A thicker 186 mm boundary layer was created using two 19 mm trips placed 2.26 m and 1.35 m ahead of the test section. Boundary layer measurements and turbulence statistics were measured and presented by Morton (2012) and Morton *et al.* (2012). They present complete measurement of the two-point cross-sectional turbulent velocity correlations at the location of the rotor plane for the undisturbed boundary layer. Statistics for the two boundary layers are shown in Table 1 for an inflow velocity of 30m/s. The boundary layer thickness was found to be nearly invariant with inflow velocity. The present study considered inflow velocities of 10m/s, 15m/s, 20m/s, and 30m/s.

Table 1. Boundary layer characteristics at rotor disk plane

δ , mm	U, m/s	C_f	δ^* , mm	θ , mm	Re_δ	Re_θ
101	30	0.00258	11.6	9.2	182,890	16,607
186	30	0.00245	19.3	15.9	345,660	29,475

B. Rotor

The rotor used in this study is the same design as used by Sevik (1971) but scaled by a factor of 2.25. A picture of the rotor mounted in the wind tunnel test section is shown in Figure 2. The rotor diameter is 457 mm with a 127 mm hub. The rotor has 10 blades with a constant chord of 57.2 mm. The blades have square tips and twist from an angle of 55.6° at the hub to 21.2° at the tip measured from the rotor plane. There is no blade sweep, lean, or skew. The design advance ratio for this rotor is 1.17 and has a zero-thrust advance ratio of approximately 1.44 calculated

using JavaProp. A 216.4 mm spinner extends forward of the base of the blades. The rotor is powered by an AKM-64P-ACCNDA00 Kollmorgen servomotor. The rotor plane was positioned 3.41 m from the entrance to the test section with a tip gap measured from the Lexan wall of 20.3mm. This results in an individual blade emersion of 50% span for the 101mm boundary layer and 100% span for the 186 mm boundary layer as it passes through the deepest point of its rotation.

C. Microphones

Noise was recorded by eight ½” Bruel & Kjaer 4190 microphones. Four microphones were positioned outside of the flow in the port chamber. These microphones had receiving angles θ_m from 53° to 90° as measured from the rotor’s axis of rotation. Another four microphones fitted with bullet nose cones were positioned in the test section and were held by aerodynamically faired stands. Two of the microphones were upstream of the rotor at 14° and 29°. They were positioned off-axis so that the wakes of the stands were not ingested by the rotor. The two downstream microphones closely mirrored the upstream inflow receiving angles and were at 151° and 169°. The inflow microphone stands stood 0.79 m tall less than half of the test section height. Therefore, they were staggered in the test section so that a microphone mounted from the floor upstream was followed by a microphone suspended from the ceiling downstream and vice versa. The location of these microphones are shown in Figure 1 and their coordinates are tabulated in Table 2 where x is the streamwise distance measured from the beginning of the test section, y is measured spanwise across from the flow at the center plane of the wall, and z is measured normal from the boundary layer surface. Figure 3 also shows a picture of the inflow and port chamber microphones. Acoustic measurements were taken at many rotor operating conditions. Tables 3 and 4 show the entire acoustic measurement test matrix. The test matrix in Table 3 was carried out for the 101 and 186 mm boundary layer cases. The test matrix in Table 4 was only carried out for the 101 mm boundary layer case. The entire test included 105 individual acoustic runs measured at all eight microphone positions.

Table 2. Location of microphones

Mic No.	x , m	y , m	z , m	θ_m , deg
1	3.42	0.76	3.59	90
2	2.69	0.80	3.38	77
3	2.17	0.79	2.96	65
4	1.70	0.80	2.50	53
5	1.25	1.04	0.80	14
6	1.31	0.79	1.42	29
7	5.52	1.05	1.43	151
8	6.15	0.79	0.80	169

Table 3. Sound measurements

RPM	10m/s	15m/s	20m/s	30m/s
1000	1.31	1.97	2.62	3.94
1500	0.87	1.31	1.75	2.62
2000	0.66	0.98	1.31	1.97
2100	0.62	0.94	1.25	1.87
2200	0.60	0.89	1.19	1.79
2300	0.57	0.86	1.14	1.71
2400	0.55	0.82	1.09	1.64
2500	0.52	0.79	1.05	1.57
2750	0.48	0.72	0.95	1.43
3000	0.44	0.66	0.87	1.31
3250	0.40	0.61	0.81	1.21
3500	0.37	0.56	0.75	1.12
3750	0.35	0.52	0.70	1.05
4000	0.33	0.49	0.66	0.98
4250	0.31	0.46	0.62	0.93
4500	0.29	0.44	0.58	0.87
3282			0.8	
1194	1.10			
1790		1.10		
2387			1.10	
3581				1.10
1367		1.44		
1823			1.44	
2734				1.44
Directivity angles from 15° to 168°				

Table 4. Sound Measurements for 2734 RPM

$U_{\infty} \text{ m/s}$	J
10	0.48
12	0.58
14	0.67
16	0.77
18	0.86
20	0.96
22	1.06
24	1.15
26	1.25
28	1.34
30	1.44
32	1.54
34	1.63
Directivity angles from 15° to 168°	

III. Results and Discussion

A. Time Averaged Rotor Sound Field

Figure 4 shows the noise spectra recorded at an inflow free-stream velocity of 20m/s for various rotor RPMs in the 101mm boundary layer as measured by microphone 4 at 53° . Rotor RPM is characterized in terms of advance ratio J , defined as the free stream velocity divided by the rotor rate of rotation in Hz multiplied by the rotor diameter. Figure 4a compares the background noise to the measured rotor noise while Figure 4b compares the noise measured from each rotational velocity by normalizing the spectra on the tip velocity to the fifth power and the blade passage frequency (BPF). In Figure 4b, the background noise has been subtracted out for each case.

From these spectra, the effect of increasing the thrust is displayed as a narrowing of the haystacks around the BPF and an increased number of haystacks, but there are also some other phenomena present in these spectra. Below the BPF, noise spikes at multiples of the shaft rotational frequency exist, specifically note the peaks at f/BPF of 0.6, 0.7, and 0.8. The high frequency lump in the $J = 1.05$ case appears to be due to vortex shedding from the blade trailing edges as discussed in the study by Hersch *et al.* (1974) for airfoils at low angles of attack. The calculated zero-thrust advance ratio for this rotor is 1.44. Therefore, at $J = 1.05$, the span of the rotor blade is at a slight angle of attack in the free stream. Of course, the angle of attack along the blade span varies as the rotor dips through the boundary layer.

The haystacks are also right weighted at higher advance ratios (see for example the first and second BPF haystacks for $J = 1.05$). The reason for this shift is diagramed in Figure 5. Haystacking noise is produced by the correlated loading of rotor blades as they slice through coherent structures. Consider two coherent structures of the same size that are inclined in different spanwise directions in relation to the rotor (red and blue) that exist in the boundary layer. These structures are then ingested by the rotor, and the blades slice them as a function of time and spanwise location. The response produced by the blue structure shown in Figure 5 will be at a frequency slightly higher than the BPF while the red is slightly lower than the BPF. However, the blue structure is cut more times. This increases the broadband noise produced by the blue structure as opposed to the red. This bias produces the right skewed haystacks at high advance ratio. As thrust is increased and the rotor begins to stretch the turbulence into its disk plane, the inclination angles of the coherent structures are reduced eliminating the right skew.

The directivity of the haystacking noise is shown in Figure 6 for different advance ratios. Shown on the -axis is the sound pressure level normalized on the inverse of the observer distance as $10 \log_{10}(\phi_{pp} r_m^2 / 4 \times 10^{-10} \text{ Pa})$.

Spectra from the downstream microphones are omitted from this figure because they strongly resemble the upstream measurements. In all cases, the broadband noise decreases towards the disk plane at 90° . The noise is not a true dipole source which would produce a null at 90° but has significant measured haystacking noise at this location due to blade twist and non-compactness of the source. Besides the existence of noise at this position, the broadband noise also decays faster than would be expected by a free field dipole. At 15° , 29° , 53° , and 90° , the expected dipole attenuations would be -0.3dB , -1.2dB , -4.4dB , and $-\infty$, respectively. Of course, this doesn't take into account the effects of reflection due to the presence of the wall.

Figure 7 shows a contour plot of the frequency spectra measured at $\theta = 53^\circ$ for a fixed rotational velocity and varying inflow velocity. Viewing the spectra and evolution of the noise this way helps to clearly identify the various sound sources and their features. Near advance ratios of 1 and 1.44, the trailing edge vortex shedding noise around 10kHz is at a maximum. Between these two advance ratios, the vortex shedding noise reduces creating a valley. The vortex shedding noise has a sharp cut-off below $J = 0.9$. As the advance ratio decreases, more haystacks gradually appear. At higher advance ratios, the right skew of the haystacks is clear particularly for the first and second harmonics which are present over the entire observed advance ratio range. In this figure, the noise produced at multiples of the shaft frequency below the BPF are also easily observed and their peak strength decreases by 10dB from $J=1$ to $J=0.5$.

Contours can also be plotted by holding the inflow velocity constant and varying RPM. Figures 8 and 9 show fixed freestream velocity contours for both the 101 mm and 186 mm thick boundary layers. The data from the four different inflow velocity conditions have been combined by normalizing the spectra on the tip velocity to the fifth power to produce single continuous contours. These contours extend from advance ratios of 0.3 to 1.9. The same features as observed in Figure 7 are observed here. The haystacks at multiples of the BPF appear as curved lines since they are no longer fixed frequencies and the vortex shedding noise around 10kHz appears again at higher J . Below an advance ratio of 0.5, the peaks at frequencies above the third BPF harmonic increase dramatically in intensity. Also, the low frequency humps at multiples of the shaft rotation frequency are again visible below the BPF.

There is remarkable similarity between the noise produced by the ingestion of the 101 mm thick boundary layer and the 186 mm boundary layers in Figures 8 and 9. These figures are nearly identical differing only in magnitude at the BPF by about 2.5dB at J higher than 0.66 which is equal to the scaling factor increase (1.8) of the boundary layer thickness. This increase comes from the ingestion of larger turbulent structures which produce a coherent response for more blade passes. This should have the effect of narrowing the haystacks and increasing the magnitude of the haystacking peaks. The larger lateral scale of the ingested turbulence may also produce a fewer number of observable haystacks. Although, clear narrowing and decreased number of haystacks are not observable in these contours. A companion study to this (Alexander *et al.* (2014)) has shown through flow visualization and direct unsteady velocity measurements that at low advance ratios, less than 0.86, the upstream boundary layer separates and the noise produced may be at least partly the result of the turbulence and mean flow disturbance generated in this separated region. Therefore, at advance ratios below this, the character of the turbulence structure may be similar between the two cases.

The noise associated with the haystacking peaks becomes partly tonal at low advance ratios. The coherence C_{Bp} of the blade clocking signal, B , with the acoustic pressure signal, p , for advance ratios of 0.33 to 1.57 was taken. The coherence is defined by Equation 1 below where ϕ_{Bp} is the cross-spectral density between the blade clocking and acoustic signals, ϕ_{BB} is the autospectral density of the blade clocking signal, and ϕ_{pp} is the autospectral density of the acoustic signal.

$$C_{BA} = \frac{|\phi_{Bp}|^2}{\phi_{BB}\phi_{pp}} \quad (1)$$

For advance ratios higher than 0.75, there was no coherence at the blade passage frequency. However, for lower advance ratios, the coherence at the blade passage frequency increases. At an advance ratio of 0.66, the coherence at the BPF is 0.4, indicating that tonal noise contributed 40% to the fundamental BPF spectral hump. This value increases to 0.7 at an advance ratio of roughly 0.45. This indicates that the spectral humps at the first harmonic shown in Figures 8 and 9 at low advance ratios have significant tonal contributions.

B. Characteristics of the Turbulence as Revealed in the Sound Field

Subtle differences in the ingested turbulent structures responsible for the haystacking noise may be observed in the acoustic signals by using a detailed analysis extending that of Alexander *et al.* (2013). A sample of the acoustic

time series taken at a free stream velocity of 30 m/s and an RPM of 4000 recorded at a receiver angle $\theta = 14^\circ$ is shown in Figure 10. The indicated areas show acoustic response believed to be created by the ingestion of coherent structures. This produces a response close to the blade passage frequency that looks similar to the burst signals observed in LDV measurements. Also indicated are areas believed to be indicative of more disorganized turbulence interaction. However, much of the time series is not labeled as it is unclear whether or not an acoustic response to an eddy passage is present. This demonstrates the importance of developing an objective method to determine the locations of significant eddy passages.

A key goal of this study is to develop a method to determine the average acoustic response to an eddy passage. This was done by determining significant eddy locations in the time-frequency domain of the individual microphone signals, averaging this instantaneous signal across multiple microphones, and then time delay-averaging successive instantaneous signals to obtain a typical representation of the acoustic signal generated by eddy structures at a given rotor operating condition. These time delay averages were then used to estimate the typical timescales of the turbulent eddies. This analysis was performed for signals generated with the thin (101-mm thick) inflow turbulent boundary layer.

As a preliminary step, the relative time delay of the rotor acoustic signals received by each of the 8 measurement microphones shown in Figure 1 was estimated. This time delay would be expected to be a function of the free stream velocity and microphone position, but not the rotor RPM. The time delay was determined relative to microphone 5's signal, since this had the highest signal to noise ratio and showed the clearest hystacking pattern at most conditions. To time-align the other signals relative microphone 5, the time-delay correlation coefficient function was computed. The correlation function is shown below in Equation 2, where p_i represents the acoustic pressure measured by the i th microphone.

$$r = \frac{\overline{p_i(t)p_5(t+\tau)}}{\sqrt{\overline{p_i(t)^2} \overline{p_5(t)^2}}} \quad (2)$$

The time delay was determined to be the time to the largest peak on the correlation function, and compared with a convection model prediction. Amiet (1978) showed that refraction through a shear layer alters the effective acoustic path from the rotor to the microphone. This alteration is given by Equations 3 and 4 below where θ_m is the actual angle of the microphone to the rotor axis consistent with Figure 1 and Table 1, r_m is the distance from the rotor to the microphone, h is the distance from the rotor to the shear layer, θ_c is the angle of the acoustic path from the rotor to the shear layer, and θ is the angle between the shear layer and the acoustic ray path after refraction. The only unknowns in Equations 3 and 4 are θ_c and θ .

The time delay calculation was carried out for assumed shear layer thicknesses of 10 and 20 cm in order to determine shear layer thickness effects. Note that

$$\tan \theta_c = \frac{\sqrt{(1-M \cos \theta)^2 - (\cos \theta)^2}}{(1-M^2) \cos \theta + M} \quad (3)$$

$$r_m \cos \theta_m = h \cot \theta_c + (r_m \sin \theta_m - h) \cot \theta \quad (4)$$

These equations are simultaneously solved for the new acoustic path angle. Convection is then accounted for and the time delay with microphone 5 is determined. Figure 11 shows, as an example, the predicted and measured time delay for microphones 3 and 4 with microphone 5, in seconds. The symbols represent time delay predicted utilizing the Amiet (1978) refraction model and accounting for convection, and the solid lines represent the time delay measured using the autocorrelation function. For all cases, as flow speed increased, the time delay with microphone 5 decreased. The predicted and measured time delays agree to within 5.5%, validating the correlation function aided time delay alignment procedure.

1. Identifying eddy ingestion events in the acoustic signals

The microphone 5 signal was used for detection of eddy passages since this appeared to provide the best signal to noise ratio. First a 100 Hz high pass ideal filter was applied to filter out the tunnel fan noise. Note that the blade passage frequency was never less than 160Hz so this had no impact on the frequencies of interest in the signal. A short time Fourier transform was then computed for the signal and the value at the blade passage frequency was taken at every time to determine the energy at the blade passage frequency as a function of time, with a 64Hz-bandwidth bin. The time window length of the STFT was thus 0.0156 seconds. This was chosen because it

completely resolved the first two BPF haystacks for all analyzed rotor RPMs (2000-4000). This time resolution corresponds to 5.2 and 10.4 blade passages for 2000 RPM and 4000 RPM, respectively.

Figure 12 shows a typical short-time Fourier transform sequence taken from one second of the 30 m/s 4000 RPM run. This run corresponds to an advance ratio J of 0.98 and a BPF of 667 Hz. Shown on the x -axis is the time in seconds and shown on the y -axis is the frequency normalized on the blade passage frequency. Structures are visible at the blade passage frequency that we believe are the result of the intermittent passage of coherent eddies through the rotor. The dark red structures indicate a higher amplitude acoustic response at the BPF, while the lighter yellow and green structures indicate lower amplitude, but still significant, acoustic responses at the BPF. One difficulty in interpreting this figure is that it is hard to distinguish individual eddies as they can be blurred together, perhaps due to simultaneous ingestion of multiple eddies.

The wavelet transform $C(a, b)$ of the acoustic pressure signal was also used in an attempt to reveal the coherent structure content of the acoustic signals. The wavelet transform is defined by Equation 5 below where $p(t)$ is the acoustic pressure, a is a scale and b is a time shift that alters the frequency and center time of a mother wavelet, φ^* . The real valued Morlet wavelet was determined to closely resemble the character of an eddy's acoustic signature and was used as the mother wavelet. The real valued Morlet wavelet is a cosine wave localized by a Gaussian window and is shown below in Equation 6.

$$C(a, b) = \int_{-\infty}^{\infty} p(t) \frac{1}{\sqrt{a}} \varphi^* \left(\frac{t-b}{a} \right) dt \quad (5)$$

$$\varphi^* = \frac{1}{\sigma\sqrt{2\pi}} e^{\frac{-t^2}{2\sigma^2}} * \cos(t) \quad (6)$$

Figure 13 shows the continuous wavelet transform for the same time signal as Figure 12. Similar to Figure 12, Figure 13 shows visible structures at the blade passage frequency (667 Hz). However, it is less difficult to distinguish individual eddies. Visibly, the structures are narrower and have more distinct start and end times.

Figure 14 shows the normalized traces of the short time Fourier transform and the continuous wavelet transform for Figures 12 and 13, respectively, at the blade passing frequency. The trace obtained from the wavelet transform was normalized to match the scale on the STFT trace, and they were found to be almost identical. This indicates that the BPF trace obtained from either the short time Fourier transform and the continuous wavelet transform both provide an objective measure of the appearance of coherent bursts in the acoustic signal due to the ingestion of eddies. The continuous wavelet transform was used for the remaining analysis due to its more distinct start and end times for eddy passages.

To obtain start and end times for eddy passages, the BPF traces of the continuous wavelet transform were analyzed. Traces were first smoothed by taking a local average of 0.008 seconds of data (512 samples) centered at each data point. This time was chosen such that it would cover at least 2.5 blade passages for the lowest RPM case analyzed. Every value below a discrimination level was then assumed to not contain a significant eddy acoustic signature. This discrimination level was set to a certain percentage of the mean trace value. Eddy passage start times were obtained from a trace's rise through the discrimination level and terminated by falling through the same level. The eddy center times were assumed to be halfway between the start and end times.

To determine the optimum discrimination level for the continuous wavelet transform analysis, the level was varied and the number of predicted eddy passages and total time in which an eddy passage occurs were plotted. Figure 15 shows the results of a typical discrimination level analysis performed on a single 10 second time record of data taken with a free stream velocity of 20 m/s and at a rotor RPM of 3500. This run was chosen because it has the most visible shelf point. Figure 15a shows the number of eddy passages detected as a function of the discrimination level. Discrimination level is plotted in terms of percentage of the mean spectral level at the blade passing frequency. Clearly, the higher the discrimination level is set, the fewer number of eddy passages is detected, but the variation is not smooth. This is because multiple eddies can pass through the rotor plane simultaneously, creating a local double hump shape in the BPF trace, which could actually increase the number of eddies detected as the discrimination level increased. Figure 15b shows the total time during which eddy passages are detected as a function of discrimination level. It is clear that the total eddy passage time smoothly decreases with increasing discrimination levels. The drop in eddy passage time is smooth because while a local double hump trace structure could increase the number of peaks with increasing discrimination level, the total time of eddy passage would still decrease. To determine the best discrimination level, the level was set at a local shelf point on the number of eddy passages plot. To objectively determine shelf points, the statistical elasticity of the number of passages with the total eddy passage time was computed. Equation 7 below shows the elasticity where T is the total eddy passage time and

N is the number of eddies detected. The statistical elasticity is a common parameter used in economic analysis. Hess (2002) describes it as the responsiveness of one variable to a change in a related variable. This is normally used to determine the response of demand to a change in price, but it was found that it also is useful for finding shelf points in the number of determined eddy plots.

$$E = \frac{dT}{dN} \frac{N}{T} \quad (7)$$

Figure 15c shows the elasticity for each discrimination level. It can be seen that there is a local shelf point on Figure 15a at a discrimination level of 150% of the mean trace. This is objectively found from the elasticity peak of 3.75 shown in Figure 15c. A similar procedure was used to determine the discrimination level for all other conditions.

2. Averaging the ingestion event acoustic signals

With the average time delay from each microphone relative to microphone 5, as well as the eddy passage center times from microphone 5, one should be able to locate the center times in the other microphones by simple time delay adjustments if every eddy passed through the rotor at the same location. However, turbulent eddies can pass through any part of the rotor disk plane immersed in the boundary layer and there will be small time delay differences. Thus, further time delay alignment is necessary. The short time local correlation function was computed for each eddy passage signal detected in the microphone 5 acoustic trace, with the corresponding signals in the other measurement microphones to determine the time delay for each eddy passage. The signal bounds on the short time local correlation function was set to 0.022 seconds. This was chosen because it is an order of magnitude higher than the highest expected time delay difference with microphone 5. It also corresponds to 7.3 blade passages for 2000 RPM cases and 14.7 blade passages for 4000 RPM cases. These bounds were large enough to encompass the majority of an eddy structure, but not so large that multiple eddies would be encompassed. This data was used to create histograms of the time delay between eddy detection events in different microphones. Figure 16 shows a typical histogram, showing the time delay between eddy passage events in microphone 5 and microphone 8 for a rotor RPM of 4000 and flow speed of 20 m/s. The histogram is assembled from a single 4 second-long time record. Shown on the x -axis is the deviation of the individual eddy time delay from the average time delay. The y -axis shows the number of eddies that had a particular time delay. It can be seen that a majority of the eddy passage time delays were equal to the average time delay, but some could vary by as much as 0.28 milliseconds or by 0.18 blade passages. Some attempt was made to use the time differences between the microphone signals determined in this way to locate in space the location of the eddy impact on the rotor disc. It was found that while the range of time delays observed was consistent with the eddy impacts in different positions on the rotor, the uncertainty of the position determination was too large to be useful. However, this could be done with a larger array of microphones including microphones located well out of the x - z plane containing the rotor.

With the time signals representing eddy ingestion events identified and time delay aligned in all the microphone signals, these signals could finally be averaged. A weighted average towards microphones with the highest SNR would benefit the clarity of the average shape, but as the acoustic directivity is dipole-like, the magnitude of the blade passage trace is already effectively cosine weighted. It was found that restricting the averaging only to signals from the in-flow microphones (mics 5 through 8) provided the cleanest time delayed averages. These time delayed average eddy passage signatures are plotted as a function of advance ratio and flow speed in Figure 17.

Figure 17 shows eddy passage signatures for J values of 0.33-1.57 and flow speeds of 10-30 m/s. The x -axes show time normalized by multiplying by U_∞/δ . The y -axes show the time delayed average acoustic pressure normalized such that the maximum is 1. The eddy passage signature corresponding to a free stream velocity of 30 m/s and a J value of 0.98 seems to have a Gaussian like decay on its amplitude, shown by a comparison to a cosine wave with a Gaussian window shown in Figure 18. This perhaps retrospectively validates the choice of the real-valued Morlet wavelet used for the continuous wavelet transform. Note that the left and right of this signature does not go to zero due to random noise. Eddy passage signatures for other conditions, corresponding to J values between 0.95 and 1.4, also display a wavelet-like form and their timewise extent appears roughly constant.

As J is reduced below 0.95, a tail like structure begins to form on the right side of the eddy passage signature, starting at an advance ratio of 0.87 for a flow speed of 20 m/s. This grows in length as the advance ratio decreases and turns into a large tonal component at an advance ratio of 0.66. Note that this tonal component is not just an increase in streamwise timescale. It extends well past the axes limits in Figure 17, and for J values less than 0.6, the

tonal component dominates the entire eddy passage signature. Analyzing the coherence of these time series with the blade clocking signal confirms a significant tonal contribution.

Figure 19 shows the time series for a low advance ratio measurement (20 m/s, 4000 RPM, $J = 0.66$). It is clear that the majority of the data is dominated by a component at the blade passage frequency. This is caused by both broadband and tonal components. Earlier analysis showed that for an advance ratio of 0.66, the BPF component had a 45% tonal component. This differs from the time series in Figure 10 which could distinguish locations of random noise. The signal in Figure 10 has no tonal component, which is confirmed by earlier coherence analysis.

The 10 m/s eddy signatures in Figure 17 agree with the trend from the 20 m/s signatures in that a tonal component becomes dominant for advance ratios of about 0.6 and lower. This tonal component may be due to the blade passing through a boundary layer separation region at the wall at low advance ratios. As stated before, Alexander *et al.* (2014) found that the boundary layer separates from the wall around the blade tips at advance ratios below 0.86. Note that this is where the tonal component on the eddy passage signatures started to form. This separation will create a mean flow variation that the rotor will ingest, resulting in tonal noise. As the advance ratio decreases, the tonal component on the right side of the eddy passage signature begins to lengthen as can be seen in the 20 m/s, $J = 0.66$ eddy signature. This may be a result of wall separation which is induced by the eddy passage. For J below 0.66, the wall separation is no longer transient and persists producing a tonal signature that dominates the entire eddy passage signature.

3. Determination of average eddy scales

Characteristic eddy time scales were estimated directly from the eddy passage signatures. First the absolute value of the eddy passage signature was taken and then the resulting shape was smoothed by locally averaging 0.003 seconds of data centered at each data point. This window was chosen such that at the lowest rotor RPM analyzed, at it would be at least one blade passage long. Next, the start and end times were determined by using a cutoff of $\frac{1}{2}$ of the peak value of the smoothed absolute value shape. The start and end time determination is shown in Figure 20. The timescales were normalized by multiplying the eddy passage time by the free stream velocity and dividing by the boundary layer thickness. The timescales are shown for varying advance ratios and flow speeds in Figure 21. No eddy passage signatures with significant tonal components were used in this analysis because there would be no clear bounds. From Figure 21, it can be seen that the normalized timescales are fairly constant at around $TU_\infty/\delta = 2.5$ and seem to increase slightly with advance ratio. This disagrees with timescales obtained from Alexander *et al.* (2013), which found that the timescales increased overall with flow speed. Within each flow speed case, the timescales decreased with an increase in advance ratio. A constant normalized streamwise timescale is more intuitive in that while the eddy is traveling faster through the rotor plane at higher free stream velocities, that eddy should be stretched at the same rate.

An error bound for the lateral scales was determined by varying the discrimination level up to 20% from the determined value and then determining the timescales from the new average eddy signatures. In order to get a conservative estimate, only 8 seconds of data was used instead of 30. The timescales were normalized by multiplying by the free stream velocity and divided by the boundary layer thickness. The standard deviation was computed for each set of normalized timescales and then averaged. This value came out to be $\sigma(TU_\infty/\delta) = 0.145$. The error bound was estimated by 2 standard deviations, or 0.29 and are shown on Figure 21. This value is roughly 11 percent.

A method to determine lateral scales using average eddy passage signatures was also developed. The time delay autocorrelation coefficient function of each eddy passage signature was computed according to Equation 8 below, where p_i represents the acoustic pressure measured by the i th microphone.

$$r_{auto} = \frac{p_i(t)p_i(t+\tau)}{\sqrt{p_i(t)^2 p_i(t)^2}} \quad (8)$$

The window for the autocorrelation function was bound by the times that corresponded where the smoothed signature was higher than $\frac{3}{4}$ of the smooth signature maximum. This was chosen subjectively and insured that only the eddy passage contributed to the correlations. A cutoff of 0.5 was set for the correlation coefficient value and the integral time scale was computed by integrating under the correlation curve. The integral timescale thus determined was multiplied by the blade speed at 95% radius and normalized on the boundary layer thickness. Figure 22 shows that the normalized timescales stay approximately constant at $TU_{R=95\%}/\delta = 0.375$. This agrees closely with Alexander *et al.* (2013) timescales obtained from using the timescale from a Gaussian fit to the haystack decay. However, more mathematical analysis on its validity is still needed. This may be due to stretching of an eddy caused

by passing through a rotor at a thrust condition occurring at the same rate as an increase in the rotor RPM. This would cause the normalized lateral timescales to remain constant.

IV. Conclusions and Future Work

The noise from a rotor ingesting a planar turbulent boundary layer has been documented over a large range of operating advance ratios. Distinct features were observed in the spectra at different advance ratios. At higher advance ratios near zero-thrust, vortex shedding was observed. Below $J = 0.9$, the shedding noise was absent. The right skewing of the haystacks at low-thrust was also observed and attributed to the preferential cutting of coherent structures turned so as to be more perpendicular to the rotor path. As the advance ratio was lowered, an increased number of haystacks were observed. These haystacks became narrower and more symmetric about the BPF. Noise produced at the BPF by the ingestion of the thicker boundary layer is approximately 2.5dB greater at higher J relating directly to the 1.8 factor increase in boundary layer thickness.

A method of detecting eddy passages from the acoustic signal was also developed using the short time Fourier and the continuous wavelet transforms. By time delay aligning the acoustic signatures from multiple microphones, time delayed average eddy passage acoustic signatures were determined for a range of advance ratios. It was found that for advance ratios between 0.75 and 1.5, the eddy passage signatures have a Gaussian window and that a tonal component was dominant for low advance ratios. This tonal component may be due the rotor ingesting mean flow variations created by boundary layer separation at low advance ratios. Streamwise scale analysis of these signatures show that their normalized timescales are roughly constant.

It was found that the blade passage frequency trace of the continuous wavelet transform agreed strongly with the short time Fourier transform, validating the use of the STFT and the CWT to objectively identify local eddy passages. This also supports the results from the average eddy passage signatures. Both the Morlet wavelet and the eddy passage signatures have the form of a sine wave with a Gaussian window.

A method for obtaining lateral timescales was also developed. Integral timescales were obtained from the autocorrelation function of the eddy passage signatures. When multiplied by the blade passage speed at 95% span and normalized on the boundary layer thickness, the normalized timescales were constant with free stream velocity and advance ratio. This agreed closely with lateral timescales obtained by Alexander *et al.* (2013)

Future analysis will be done to further evaluate streamwise lateral timescales. The effect of variation of the timescale of the Gaussian window of the Morlet wavelet will be studied. Setting the timescale to that of the average eddy passage signature should result in the CWT having a larger magnitude at the blade passage frequency during an eddy passage relative to the average magnitude. Variation from this timescale should allow for verification of the results in Figure 21, and produce results with much lower uncertainty.

Alexander *et al.* (2013) determined the lateral scale of the eddies by fitting a Gaussian to the haystacking peak decay. One problem with this method is that the Gaussian fit only matched well with the first two haystacking peaks. This will be expanded upon more accurately by fitting a sum of Gaussians to the haystacking decay and insuring that all peaks are included by the Gaussian fit. An integral timescale will be obtained from the resulting Gaussian fit.

Acknowledgments

The authors would like to thank the Office of Naval Research, in particular Drs. Ki-Han Kim and John Muench, for their support under grant N00014-10-1-0908 and N00014-14-1-0141.

References

Alexander, W. N., Devenport, W., Morton, M. A., and Glegg, S. A. L., "Noise from a Rotor Ingesting a Planar Turbulent Boundary Layer", 19th AIAA/CEAS Aeroacoustics Conference, May 27-29, 2013, Berlin, DE, AIAA-2013-2285.

Alexander, W. N., Devenport, W., Wisda, D., Morton, M., and Glegg, S. A. L., "Sound Radiated from a Rotor and Its Relation to Rotating Frame Measurements of Ingested Turbulence", *to be presented at the 20th AIAA/CEAS Aeroacoustics meeting in Atlanta, Georgia June 16-20, 2014.*

Amiet, R.K., 1978, "Refraction of Sound by a Shear Layer" *Journal of Sound and Vibration*, vol. 58, Issue 4, pp. 467-482

Hess, Peter. *Using Mathematics In Economic Analysis*. Upper Saddle River: Prentice Hall, 2002. Print.

Majumder, S. and Peake, N., 1998, "Noise Generation by the Interaction between Ingested Turbulence and a Rotating Fan", *Journal of Fluid Mechanics*, vol. 359, pp. 181-216.

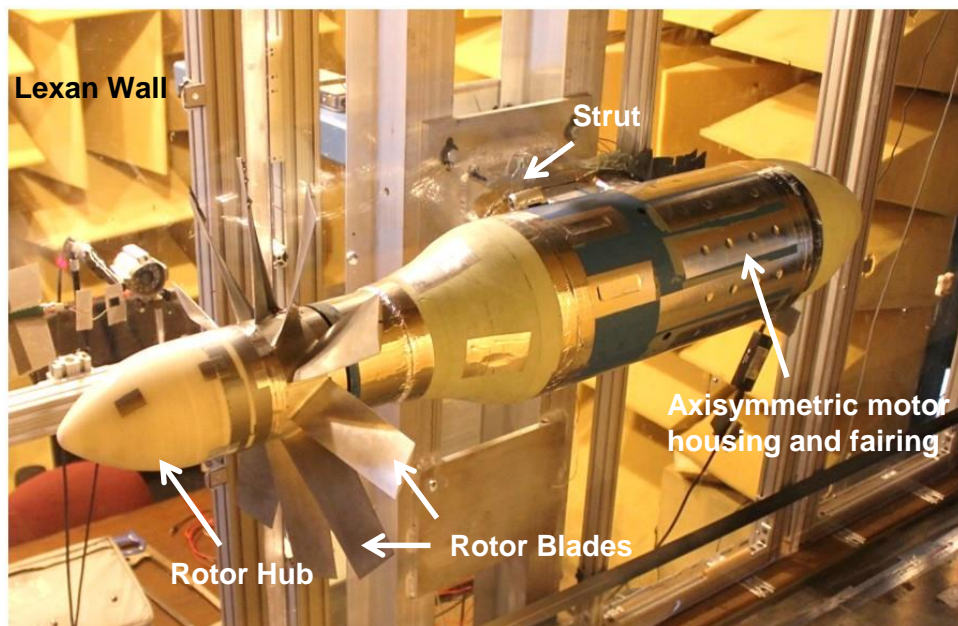
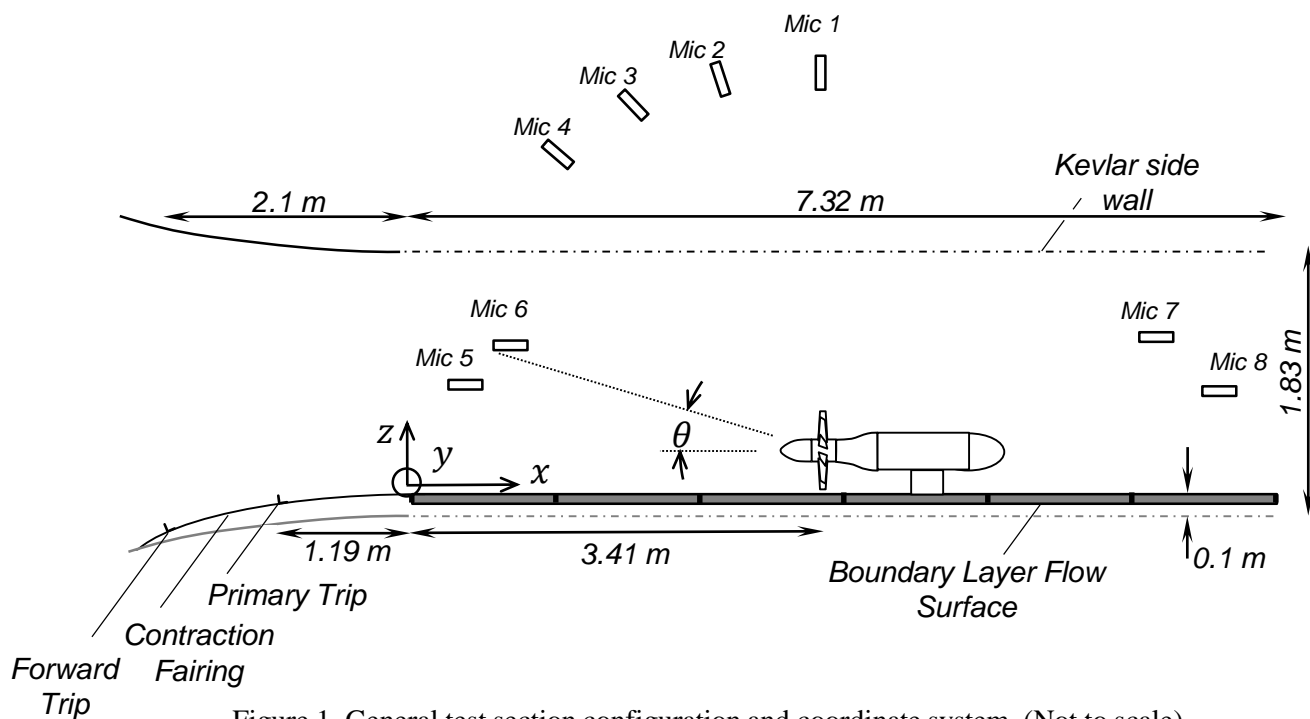
Meyers, T., Alexander, W. N., Devenport, W., and Glegg, S. A. L., "High Reynolds Number Turbulent Boundary Layer Flow over Rough Walls: Wall Pressure Spectrum and Noise", 19th AIAA/CEAS Aeroacoustics Conference, Berlin, DE, May 2013, AIAA-2013-2249.

Morton, M. A., 2012, "Rotor Inflow Noise Caused by a Boundary Layer: Inflow Measurements and Noise Predictions", Master's Thesis, AOE Department, Virginia Tech, Avail: <http://scholar.lib.vt.edu/theses/available/etd-08102012-103032/>.

Morton, M., Devenport, W., Alexander, W. N., Glegg, S. A. L., and Borgoltz A., "Rotor Inflow Noise Caused by a Boundary Layer: Inflow Measurements and Noise Predictions", 18th AIAA/CEAS Aeroacoustics Conference, Colorado Springs, CO, June 4-6, 2012, AIAA-2012-2120.

Sevik, M., "Sound Radiation from a Subsonic Rotor Subjected to Turbulence", 1971, NASA SP 304.

Stephens, D. and Morris, C., 2009, "Sound Generation by a Rotor Interacting with a Casing Turbulent Boundary Layer", *AIAA Journal*, vol. 47, pp. 2698-2708.



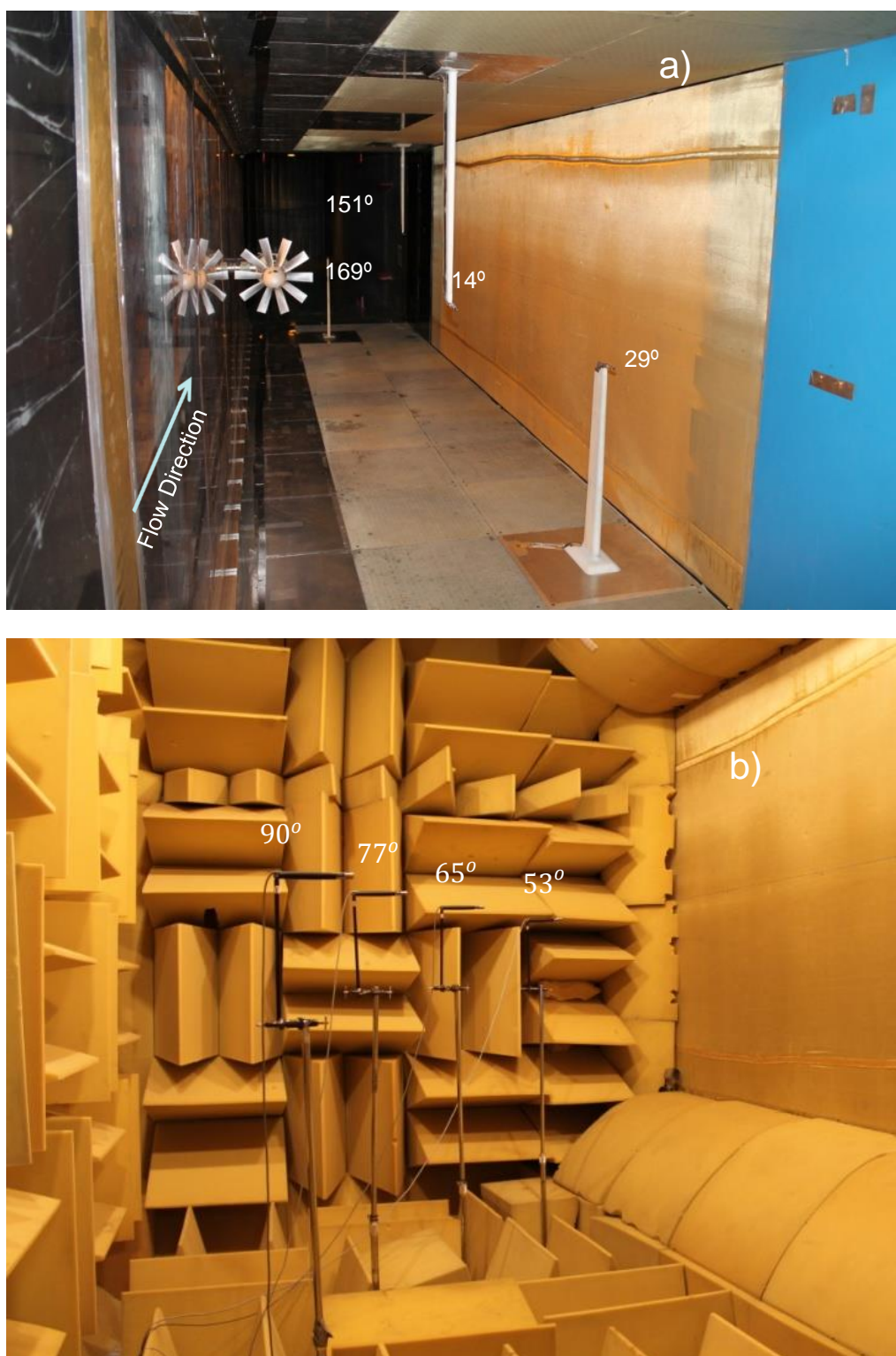


Figure 3. a) Inflow microphones b) and port chamber microphones

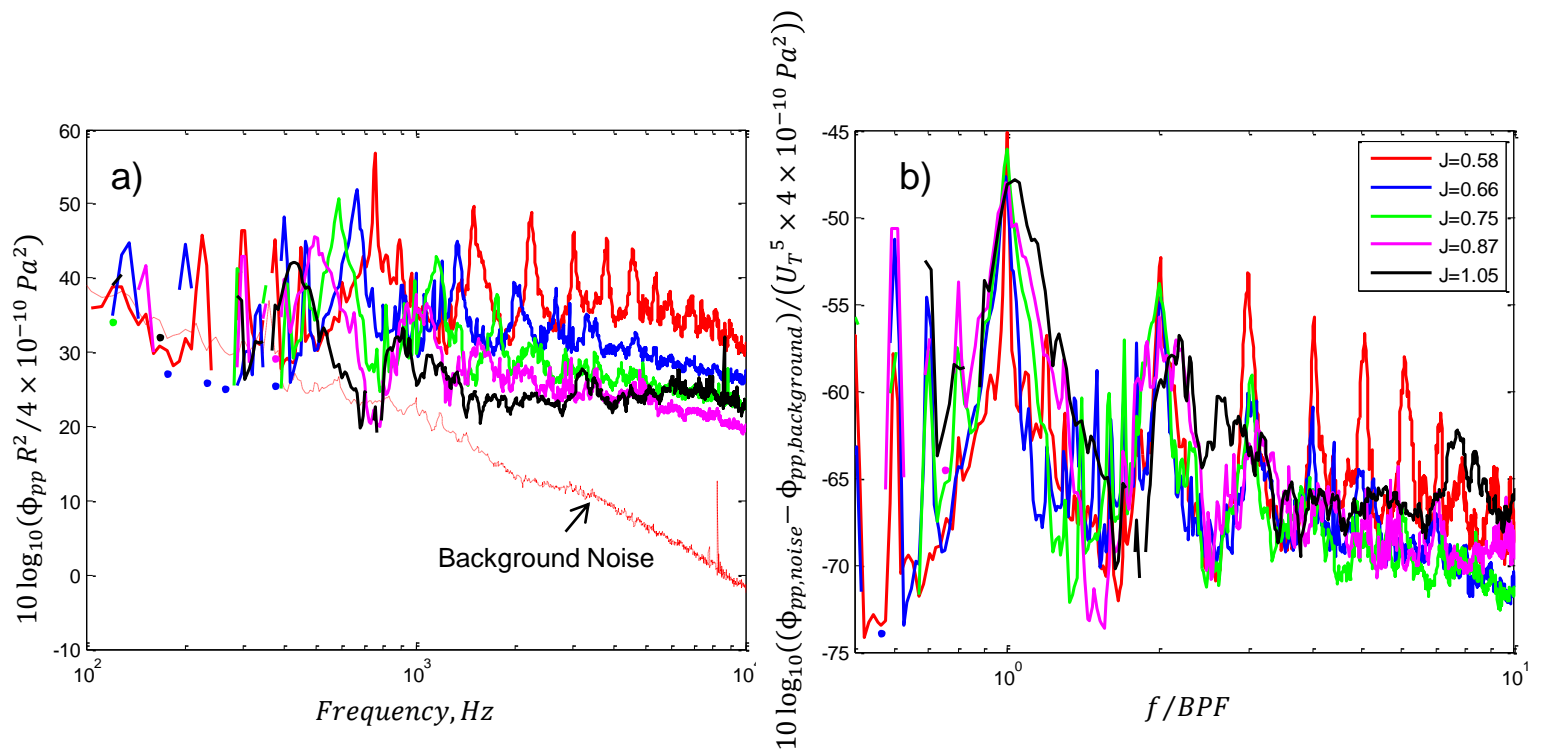


Figure 4. Rotor noise at $U_o = 20\text{m/s}$ for various advance ratios J a) compared to background noise b) and normalized on the tip velocity and BPF

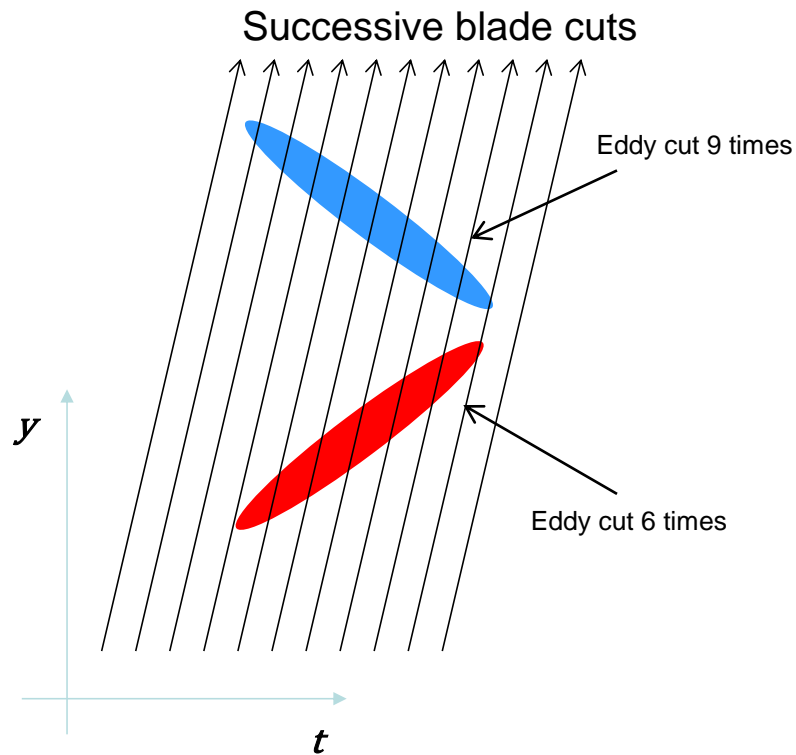


Figure 5. Diagram of explanation of right-skewed haystack at high advance ratio

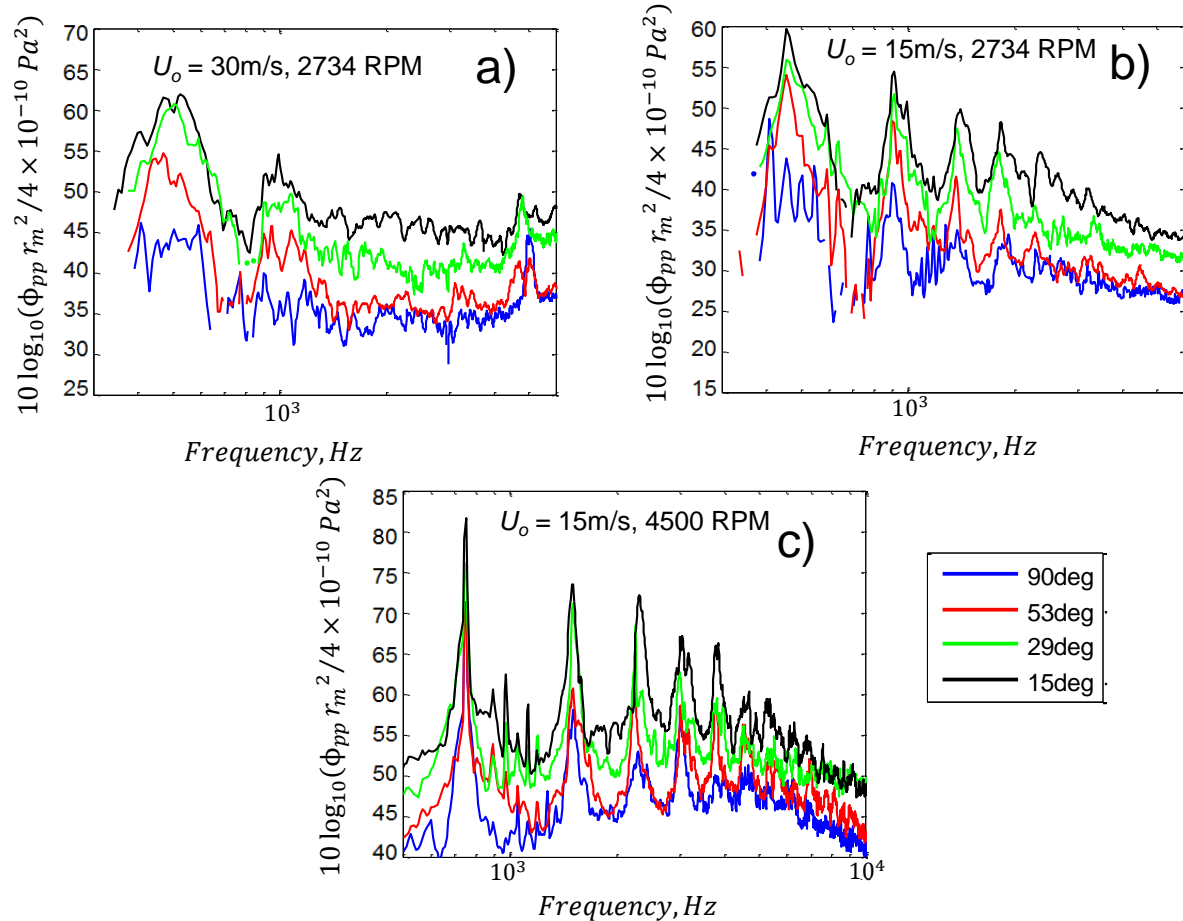


Figure 6. Directivity of noise at a) $J=1.44$, b) $J=0.72$, c) and $J=0.44$

Blue-skewed haystacks
narrow with decreasing J

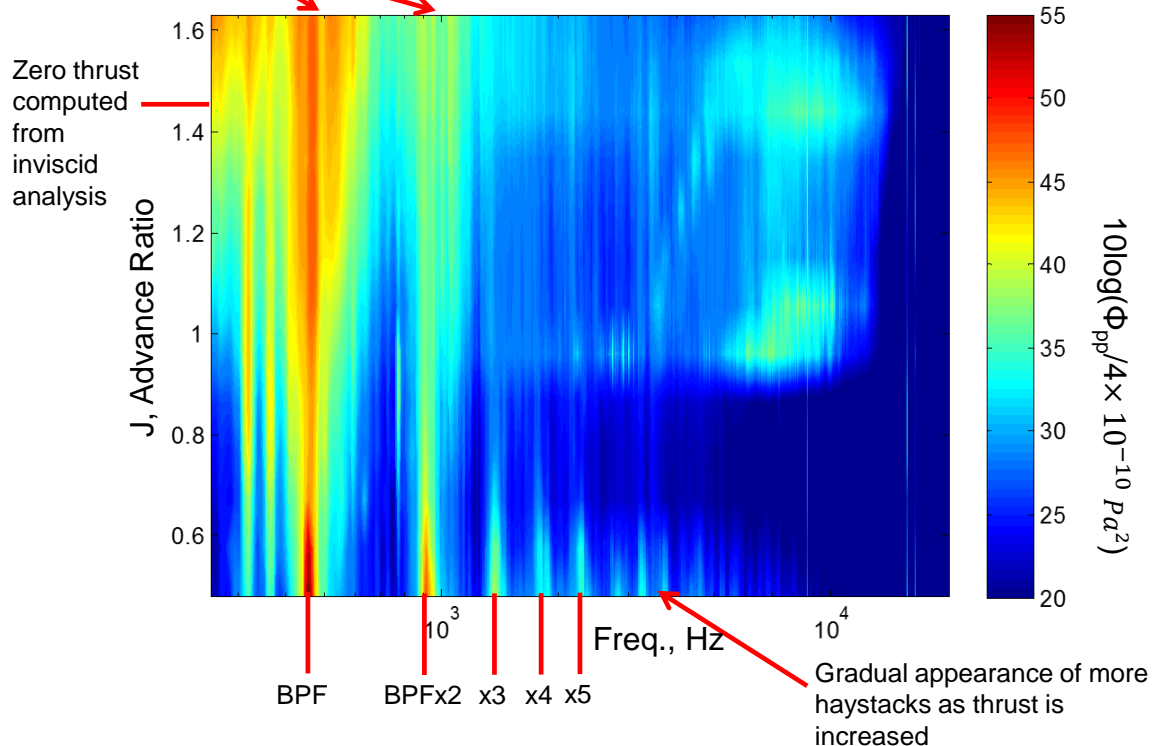


Figure 7. Contour of noise spectra over a range of advance ratios at fixed RPM of 2734 and varying inflow speed (measured at 53°)

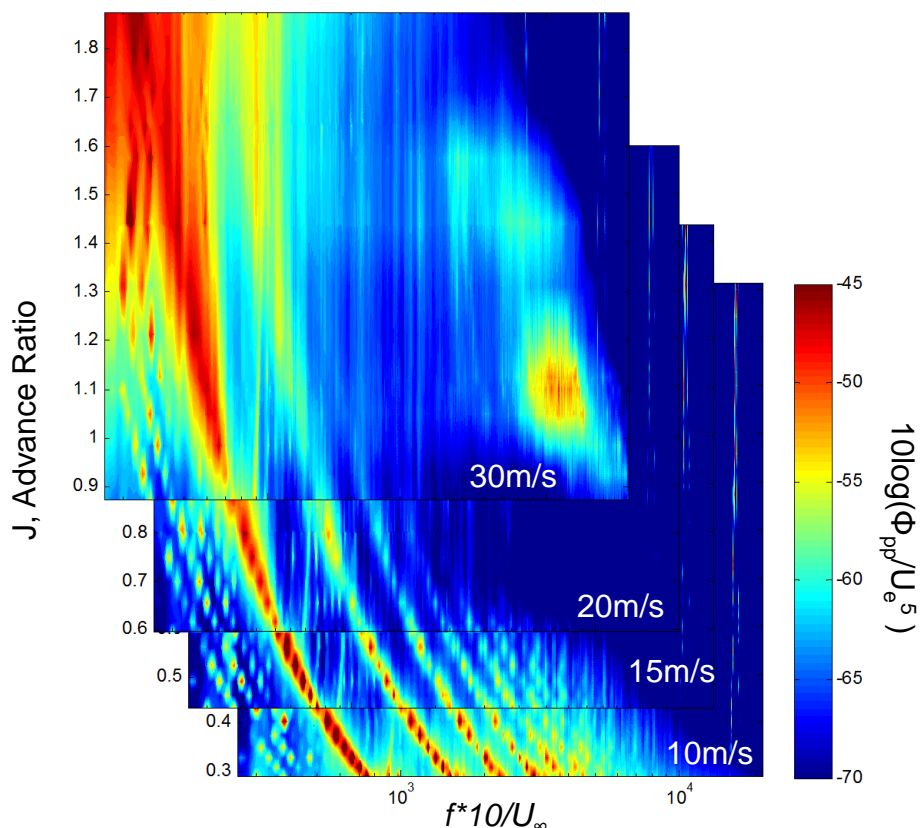


Figure 8. Combined contours of noise spectra over a range of advance ratios at fixed inflow velocities and varying RPM normalized on tip velocity for the 101 mm boundary layer (measured at 53°)

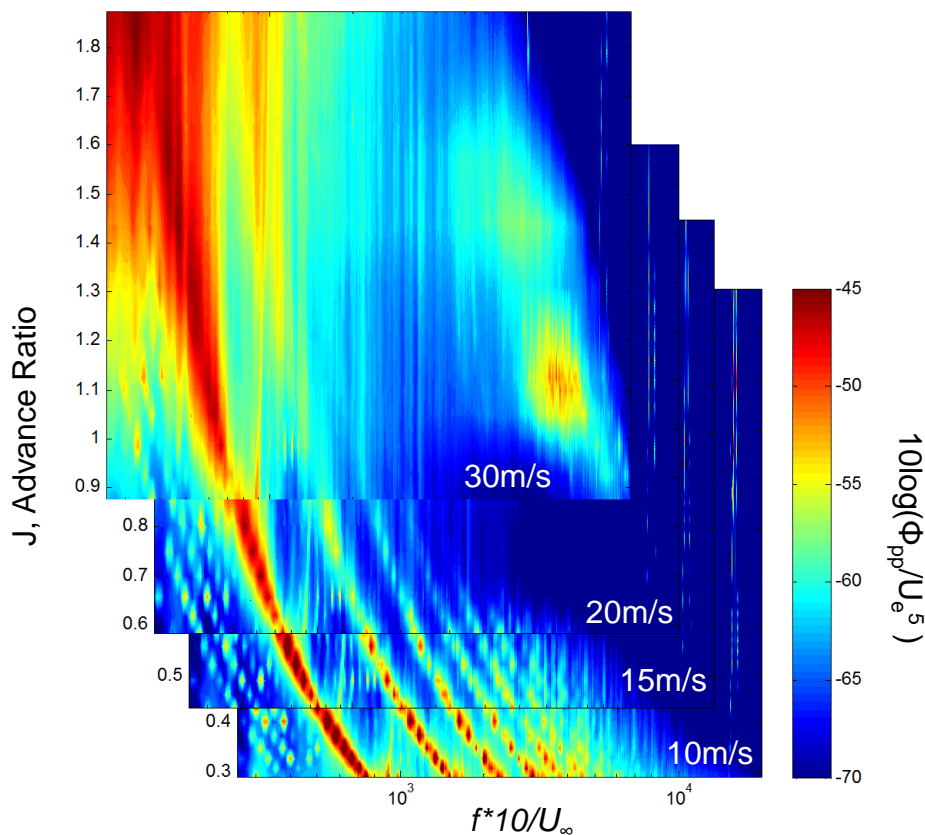


Figure 9. Combined contours of noise spectra over a range of advance ratios at fixed inflow velocities and varying RPM normalized on tip velocity for the 186 mm boundary layer (measured at 53°)

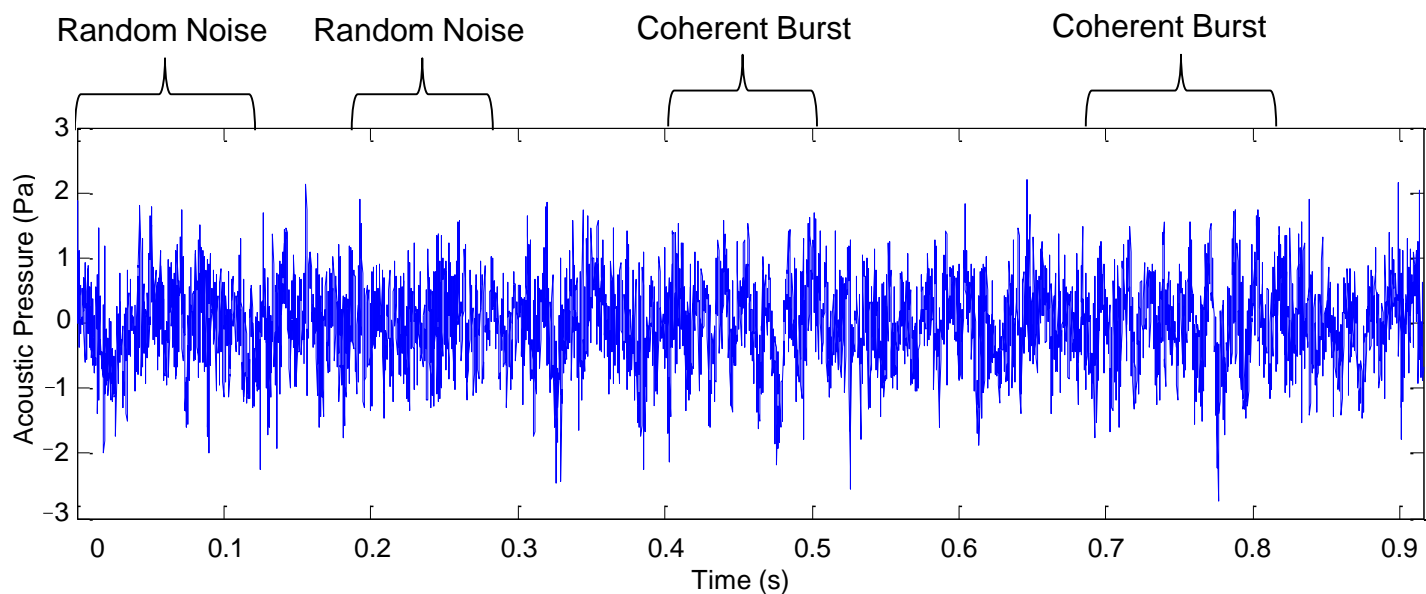


Figure 10. Time series of noise showing bursts as coherent structures are cut by successive blades
(30 m/s, 4000 RPM, $J = 0.98$, $\theta_m = 14^\circ$)

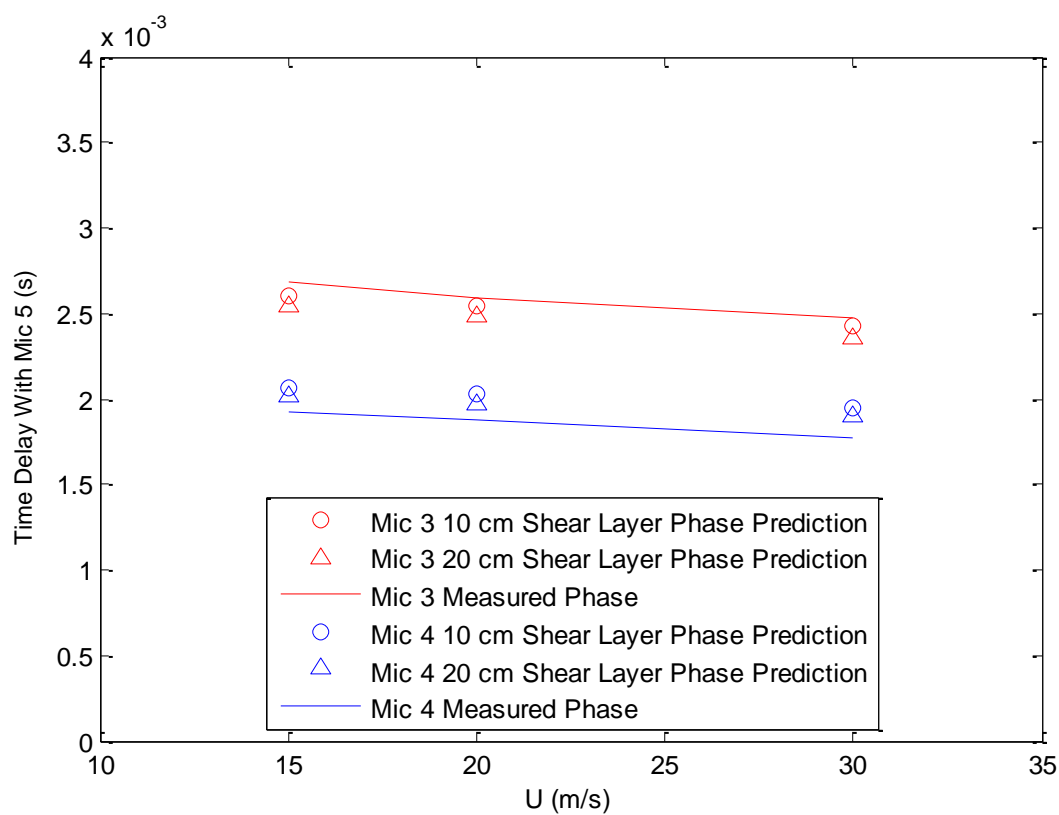


Figure 11. Measured and Predicted Full Signal Time Delays of Microphones 3 and 4 with Microphone 5

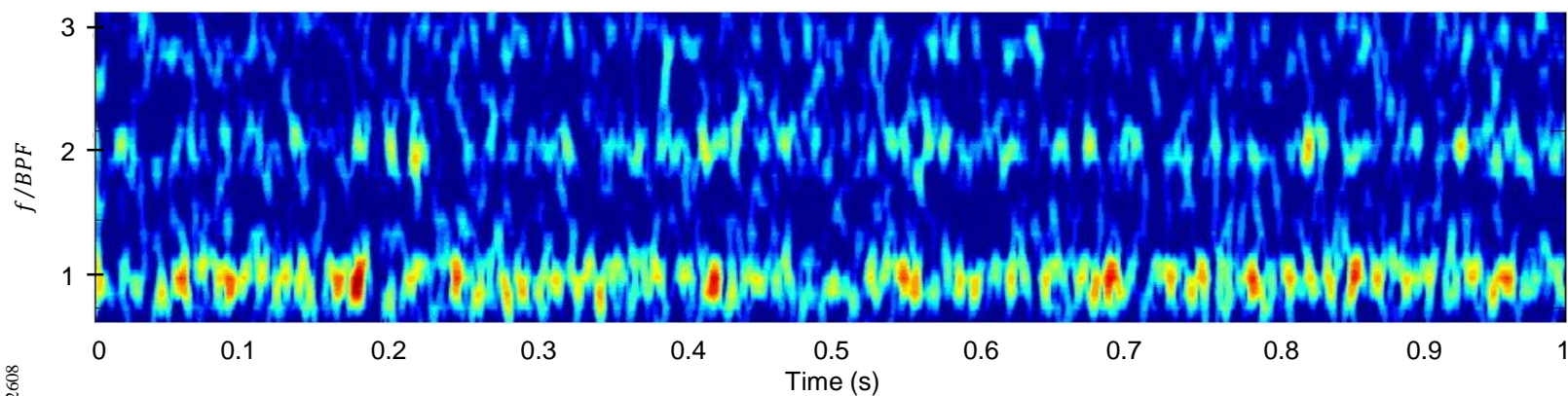


Figure 12. Short-Time Fourier Transform of acoustic signal ($U_{\infty} = 30m/s$, 4000 RPM, BPF = 667 Hz)

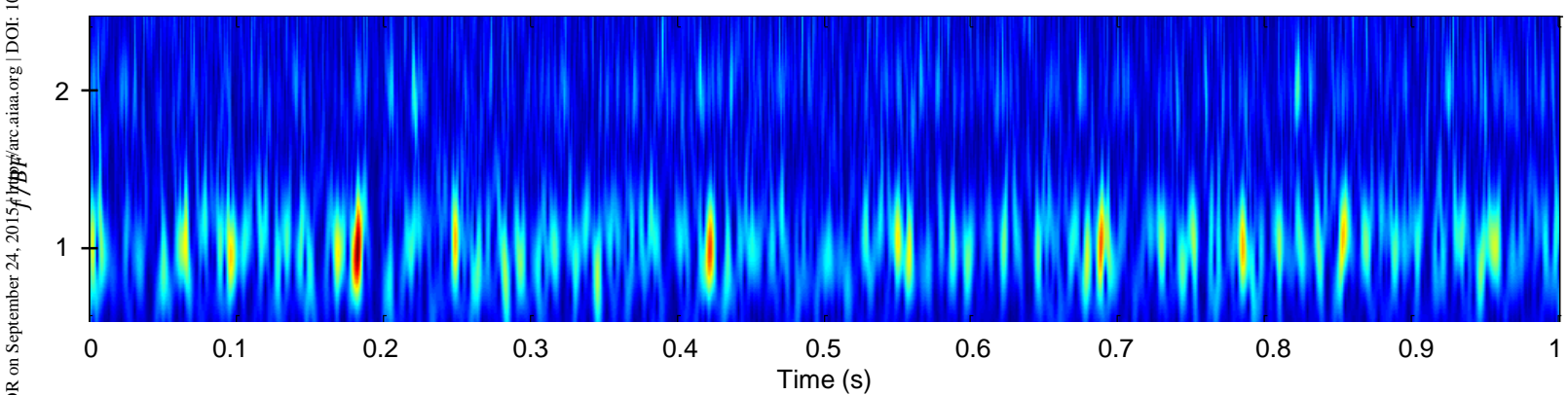


Figure 13. Continuous Wavelet Transform of acoustic signal $U_{\infty} = 30m/s$, 4000 RPM, BPF = 667 Hz)

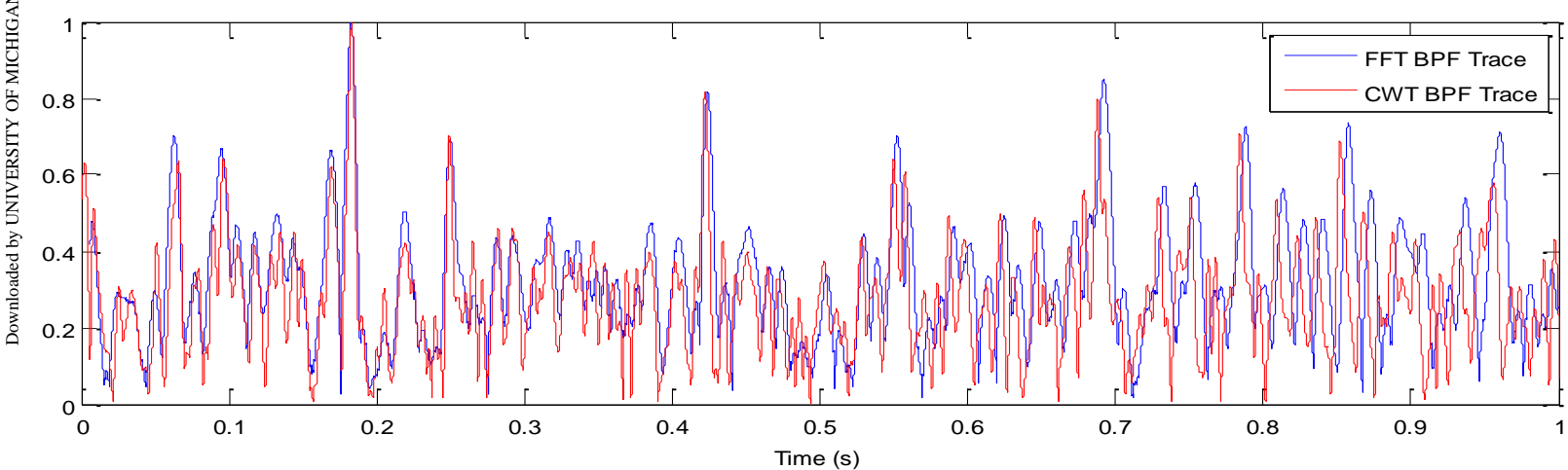


Figure 14. BPF Traces of Continuous wavelet transform and short time Fourier transform of acoustic signal ($U_{\infty} = 30m/s$ and 4000 RPM)

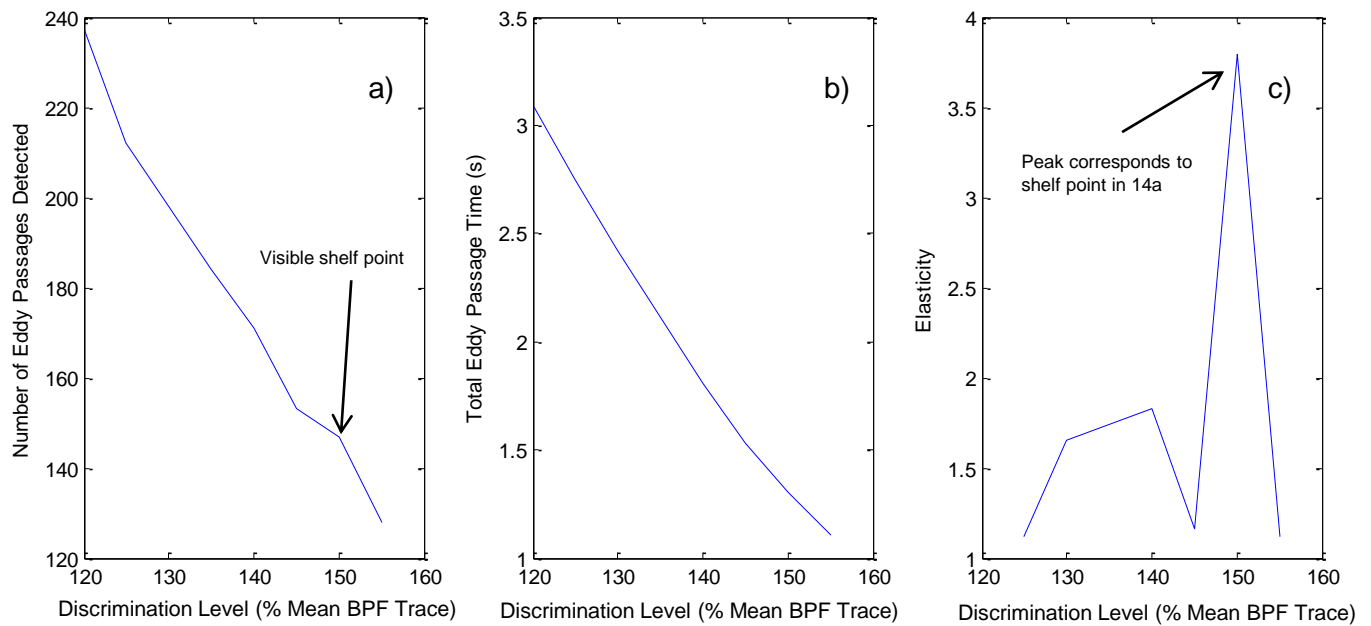


Figure 15. Effects of discrimination level on a) Number of eddies detected, b) Total time of eddy passage, and c) Elasticity of number of eddies detected with total time of eddy passage. (20 m/s, 3500 RPM)

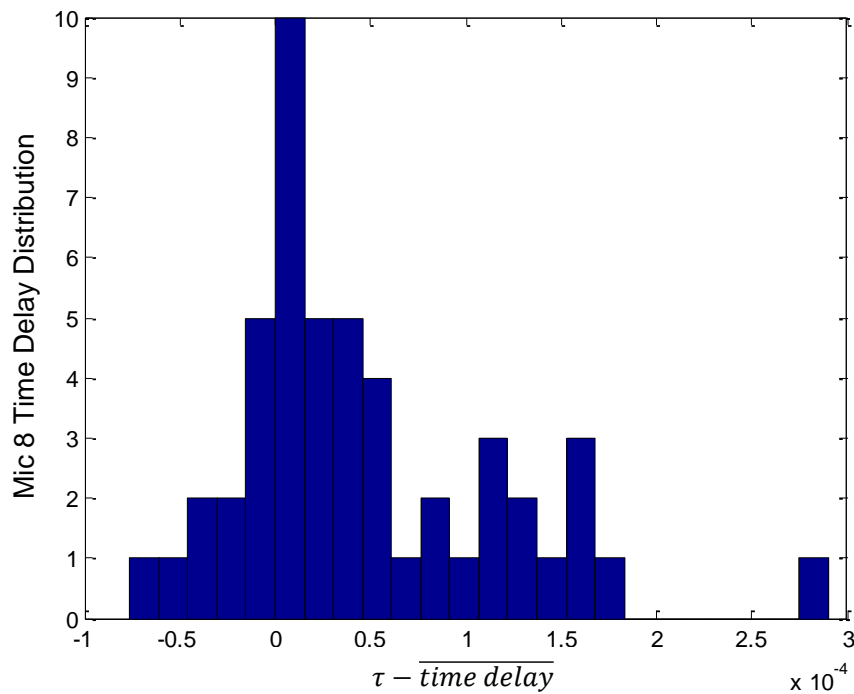


Figure 16. Typical deviation of differences in individual eddy arrival times of microphone 5 and microphone 8 for $U=20$ m/s and $RPM = 4000$ over a 4 second interval.

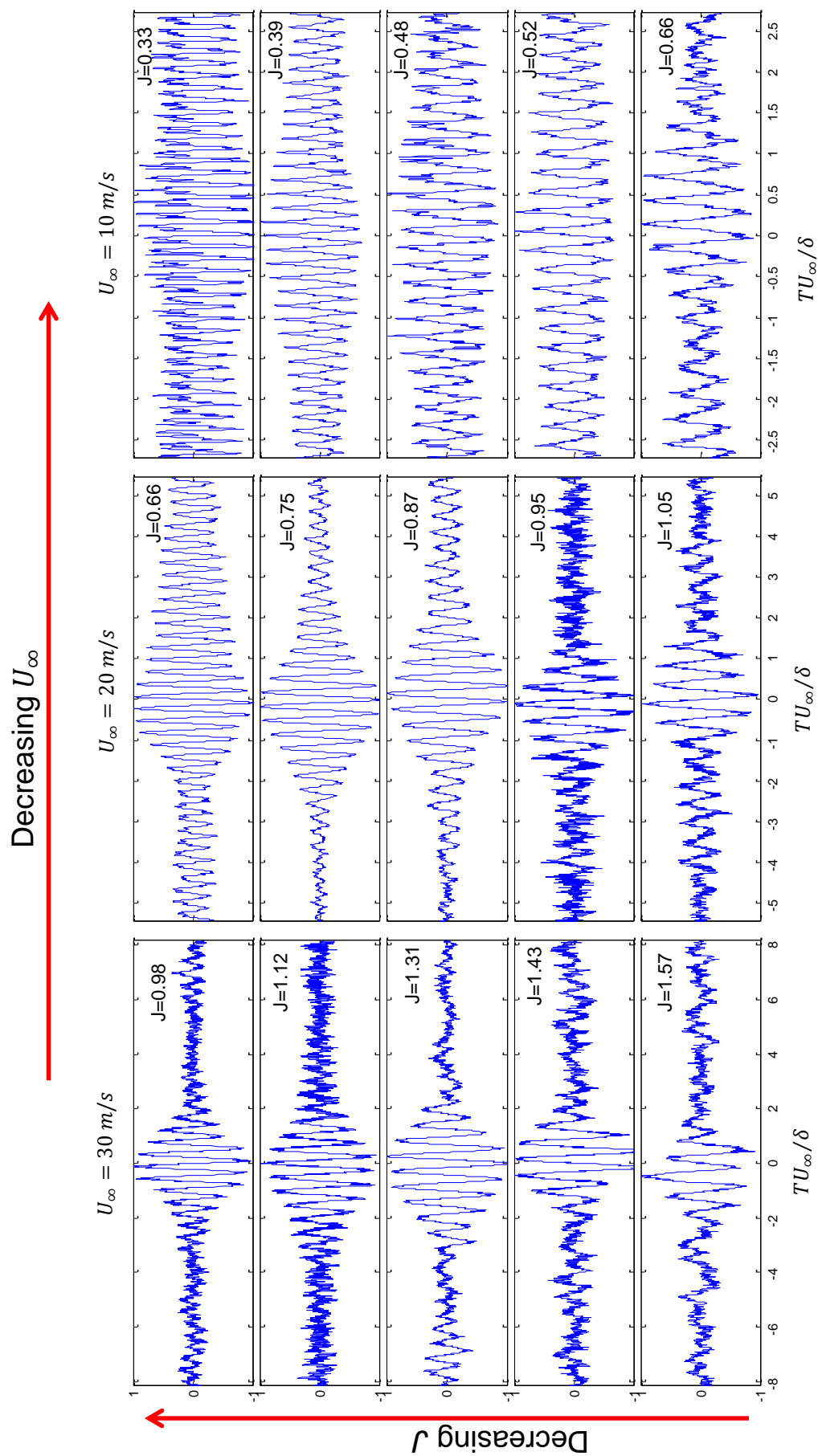


Figure 17. Phase averaged eddy passage acoustic signatures for 30, 20 and 10 m/s at advance ratios of 1.57 to 0.98.

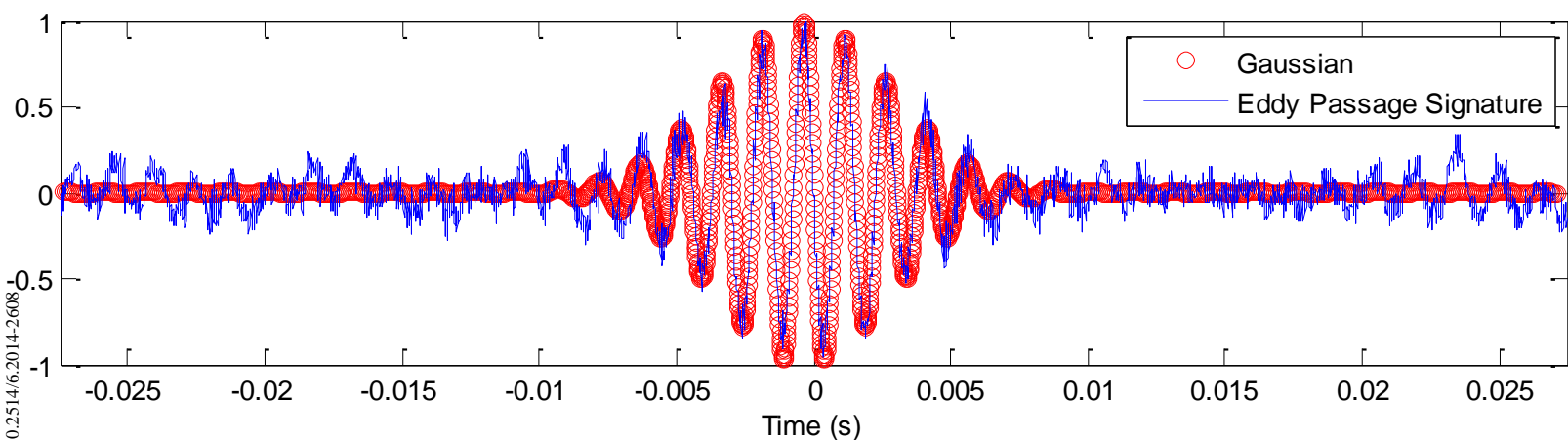


Figure 18. Comparison of a cosine wave with a Gaussian decay to the average eddy passage signature for $U_{\infty} = 30 \text{ m/s}$, $RPM = 4000$, and $J = 0.98$

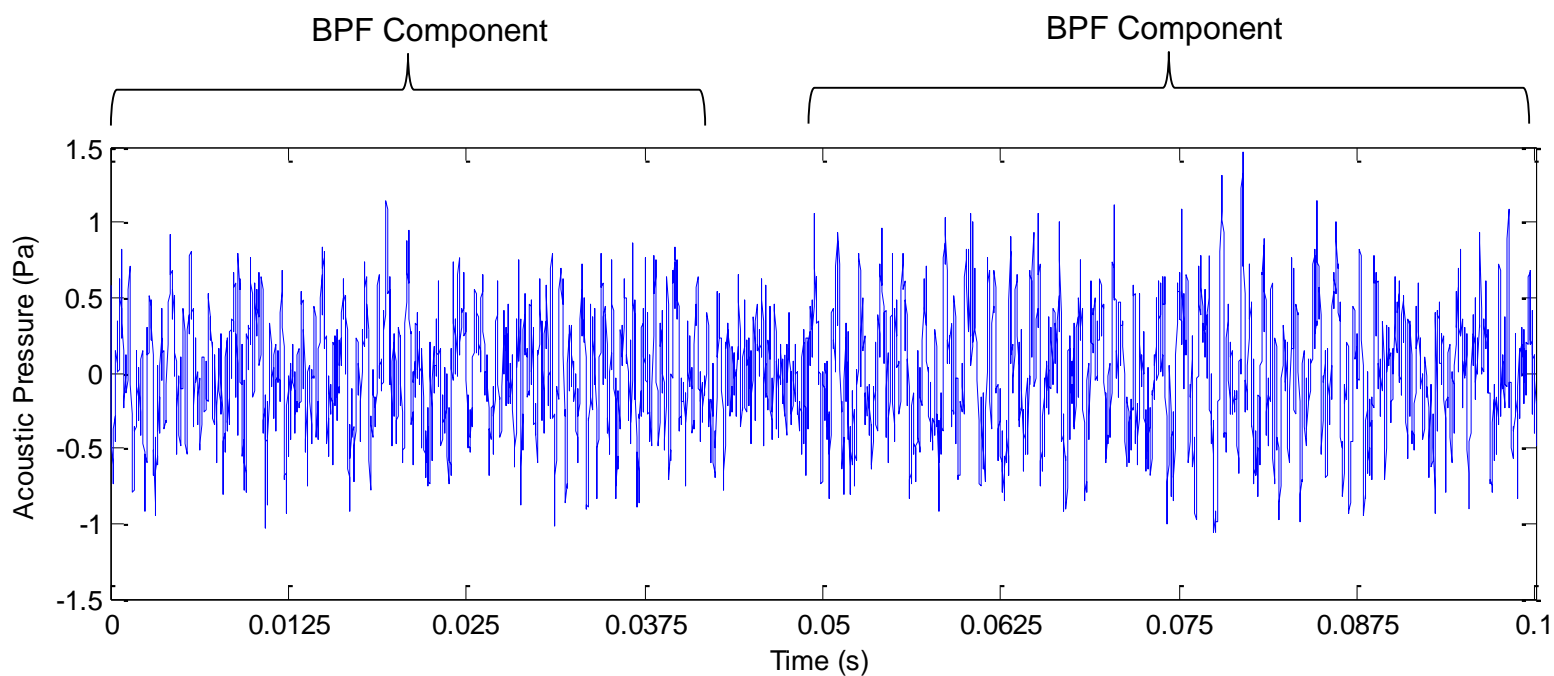


Figure 19. Acoustic pressure time series for $U_{\infty} = 20 \text{ m/s}$, $RPM = 4000$, $J = 0.66$, showing a dominant signal component at the BPF. (Taken at $\theta_m = 14^\circ$)

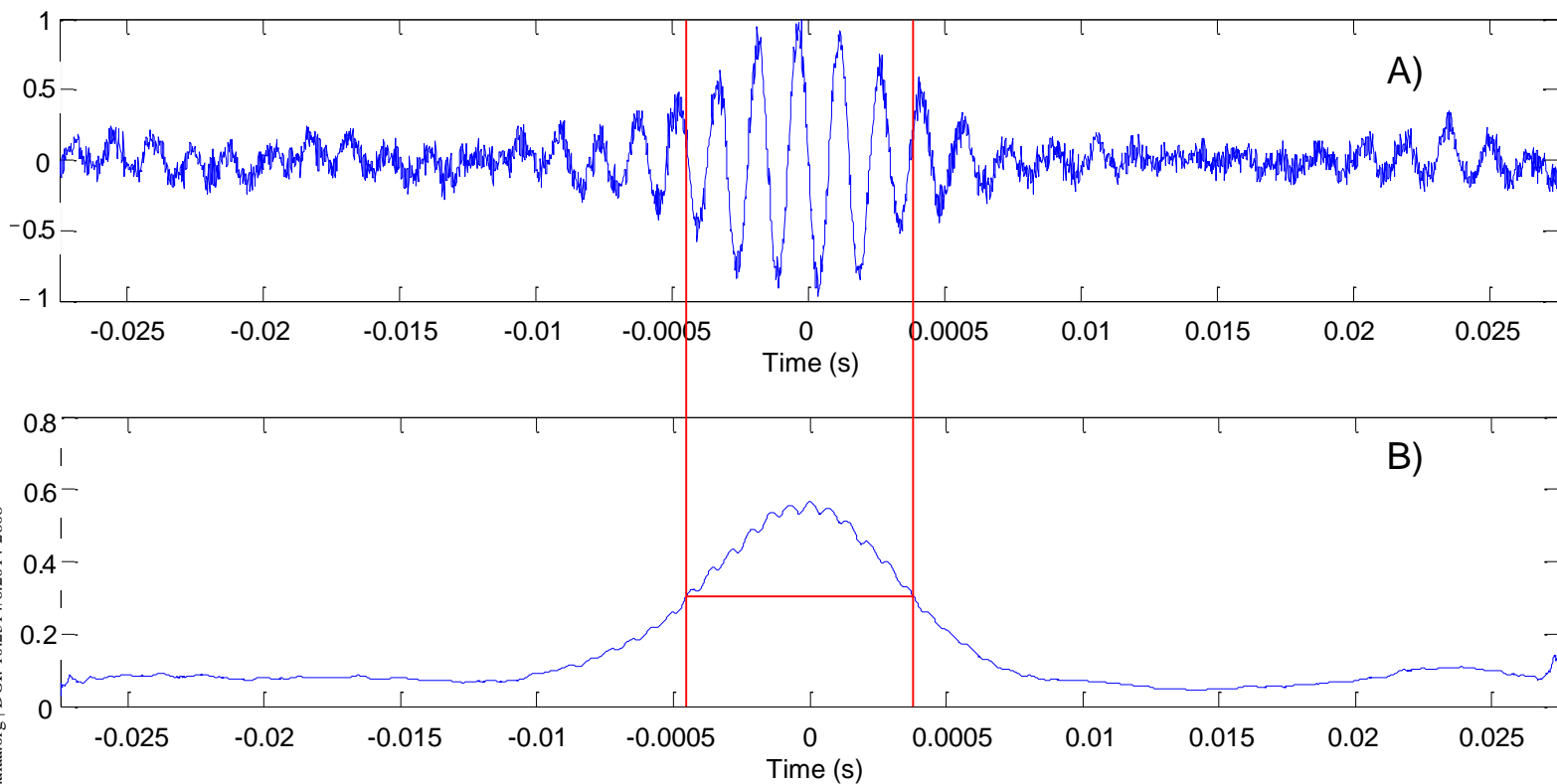


Figure 20. Determination of the eddy streamwise lengthscale for a 30 m/s 4000 RPM case by evaluation of the smoothed absolute value of the average eddy passage signature. Note, 21a) is the average eddy passage signature and 21b) is the smoothed eddy passage signature.

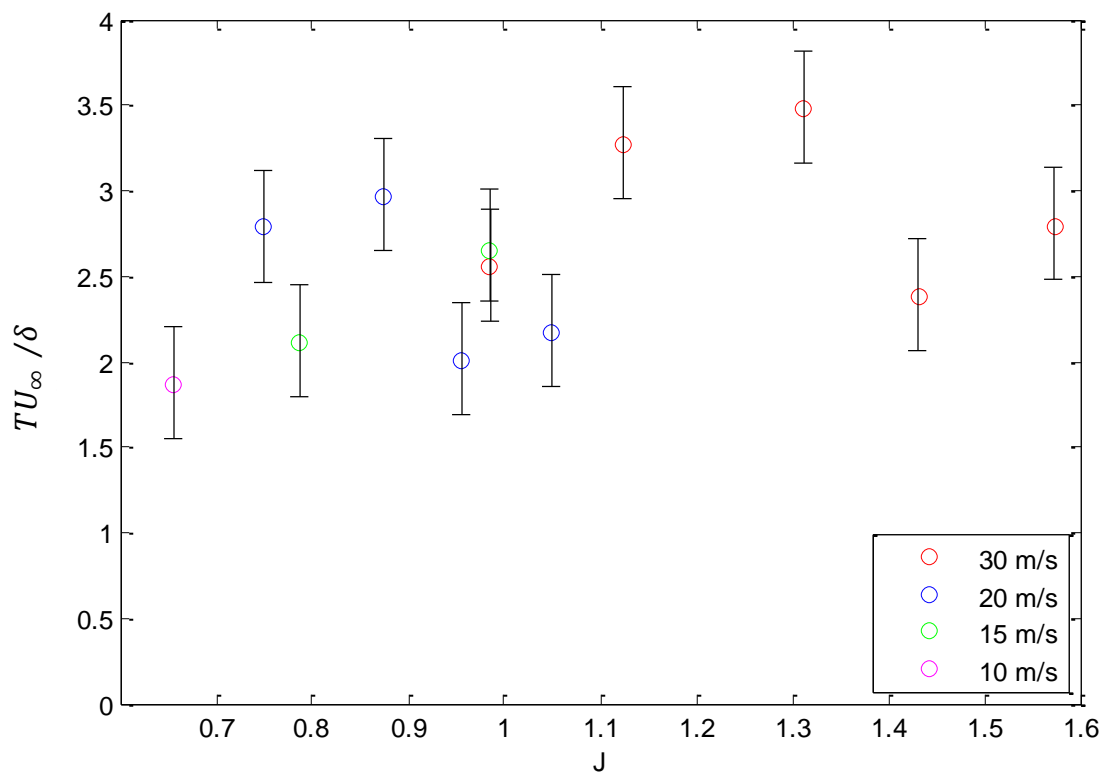


Figure 21. Streamwise scales obtained directly from average eddy passage signatures for varying advance ratios and free stream velocities.

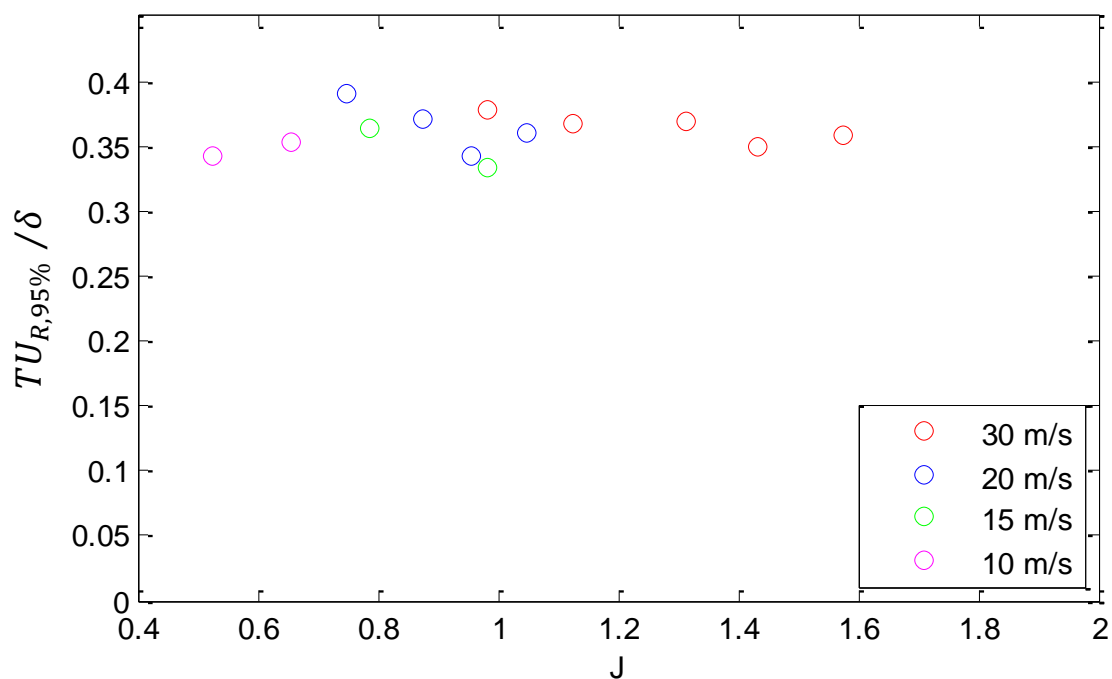


Figure 22. Lateral scales obtained from the integral timescales of the average eddy passage signatures' autocorrelation functions for varying advance ratios and free stream velocities.